

TokEye: Fast Signal Extraction for Fluctuating Time Series via Offline Self-Supervised Learning From Fusion Diagnostics to Bioacoustics

Nathaniel Chen Kouroche Bouchiat Peter Steiner Andrew Rothstein
 David Smith Max Austin Mike van Zeeland Azarakhsh Jalalvand
 Egemen Kolemen

February 27, 2026

Abstract

Next-generation fusion facilities like ITER face a "data deluge," generating petabytes of multi-diagnostic signals daily that challenge manual analysis. We present a "signals-first" self-supervised framework for the automated extraction of coherent and transient modes from high-noise time-frequency data across a variety of sensors. We also develop a general-purpose method and tool for extracting coherent, quasi-coherent, and transient modes for fluctuation measurements in tokamaks by employing non-linear optimal techniques in multichannel signal processing with a fast neural network surrogate on fast magnetics, electron cyclotron emission, CO₂ interferometers, and beam emission spectroscopy measurements from DIII-D. Results are tested on data from DIII-D, TJ-II, and non-fusion spectrograms. With an inference latency of 0.5 seconds, this framework enables real-time mode identification and large-scale automated database generation for advanced plasma control.

1 Introduction

Understanding the complex internal state of a tokamak relies on interpreting a vast array of diagnostic signals. These signals can help scientists identify the plasma's operational state, transient events,

and potentially damaging disruptions. Key classes of these phenomena, including coherent modes such as magnetohydrodynamic (MHD) instabilities and Alfvén eigenmodes (AE), and transient modes such as edge localized modes (ELM) and neutral particle spikes, manifest as fluctuations, typically in frequencies ranging from 0 to 250kHz [1, 2, 3, 4]. These events are best analyzed in the time-frequency domain, where their spectral signatures contain rich information about the plasma's state.

However, consistently extracting these signatures presents a formidable challenge. Tokamak measurements can be inundated with high levels of stochastic and integrated noise as well as overlapping transient burst events that can obscure measurements of coherent modes. This often removes faint but physically significant events, rendering simple threshold-based identification methods ineffective. Consequently, scientists and engineers must rely on time-consuming manual post-processing and color mapping or a set of filterbanks designed for each set of specific diagnostics to identify events of interest, scouring logs and large datasets for specific shots. With so many methods of data processing, this analysis bottleneck not only slows the pace of physics discovery but can also restrict data labeling in fusion, a critical prerequisite for training modern artificial intelligence (AI) models as most efforts in time-frequency (TF) data annotation has focused on either broad location an-

notation or annotation of very specific events in small datasets without a unified annotation method. This challenge is becoming critical. As the fusion community progresses towards burning plasma regimes, data volume rapidly grows; facilities like ITER are projected to generate over a petabyte of data daily [5].

AI has previously assisted in identifying plasma phenomena [6, 7]. Solutions for mode identification have explored prior-based mode segmentation [8, 9] and a neural-network based unsupervised database creation from magnetic diagnostics [10]. However, these methods are often deployed on sensors that resolve stationary signals with little white noise. Developing a method that works across multiple types of sensors is difficult. Alternatively, manually annotated and simulation-based datasets induce a bias towards well-modeled phenomena and may fail to generalize to novel plasma scenarios or new diagnostics. In addition, these algorithms may be computationally expensive, making them difficult for real-time analysis.

The rest of the paper is organized as follows: In Section 2.1, we develop a taxonomy of generally observed signal types. Next, we use a self-supervised method to automatically create the labeled dataset that surrogate model can train on across a wide range of different diagnostics. This includes incorporating an automated baseline identification for unified broadband turbulence and TF-impulse separation without explicit labels in Section 2.3, a non-linear multichannel cross-spectrum inspired self-supervised signal enhancement in Section 2.4, robust thresholding for spectrograms in Section 2.5, and label correction in Section 2.6. We detail the development of this process and demonstrate its capabilities by employing surrogate machine learning models for direct interpretable event analysis. This is demonstrated on four representative case studies: electron cyclotron emission (ECE), Carbon Dioxide based interferometers (CO₂), Magnetics High Resolution (MHR), and beam emission spectroscopy (BES) [11, 12, 13, 14].

2 Methods

We approach this task with the goal of being able to cleanly separate potential signals of interest directly from a background. In order to develop a general algorithm that works across a broad range of fluctuation measurements, a signals-first approach to data extraction is preferred since there can be a variety of physically observed signals that are sparsely described throughout literature. Constructing a labeled fusion database requires distinguishing physical signals from noise. However, fusion diagnostics can contain superpositions of many phenomena not limited to tearing modes (TM), AE, ELM, broadband turbulence, power injections, antenna scans, and thermal fluctuations which blur the boundary between signal and noise [15]. In addition, some phenomena can only be observed on specialized diagnostics. Therefore, it is necessary to distinguish general classes of signals based on their characteristics and in a method as agnostic to the sensor-type as possible.

2.1 Defining a general taxonomy of signals

To our knowledge, while it is widely known in the fusion community, there has been no single formalized taxonomy of observed fusion-based signals yet that we can reference as a means of separating signals into components. Therefore, we propose to develop one based on the physical behavior of nonstationary time series and diagnostics. Time series can be classified into deterministic and random processes, with deterministic processes classified as periodic and non-periodic while random processes can be classified as stochastic and non-stochastic processes [16]. For the goal of spectrogram visualization, we categorize these signals into five distinct classes: coherent, quasi-coherent, transient, broad, and stochastic measurements, with coherent and quasicohherent modes sharing a general category of coherent measurements, transient and broad events sharing a category of broadband measurements, and stochastic measurements in the category of noise. A summary can be found in Figure 1.

Since deterministic periodic behavior arises from

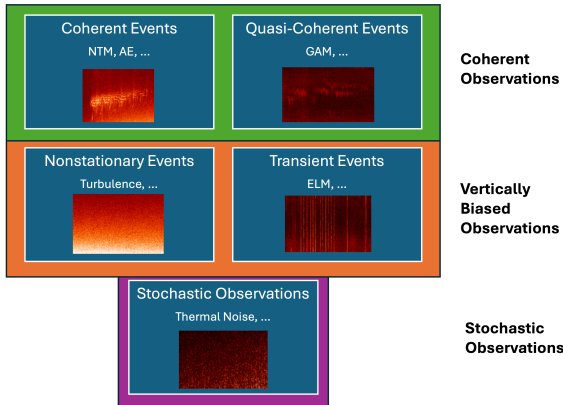


Figure 1: Signal taxonomy with example modes and spectra.

resonance at specific energy levels, we can define these as having a well-defined frequency at a point in time. This is often the principal signal measured in magnetic measurements, as they measure changes to the equilibrium state of the plasma. By doing so, it comes with the benefit that the signal by default will give clean frequency bands. However, the frequency need not be the same over time. Changes in energy distribution can lead to chirping structures, which is well observed in many fields. Therefore, we can relate this general class of signals to our understanding of coherent modes in fusion, where narrowband characteristics persist over a certain amount of time. These can include neoclassical tearing modes (NTM), geodesic acoustic modes (GAM) TM, AE, and kinks.

Nonperiodic deterministic behavior can be described as deterministic changes in measurements, such as global changes in current or density over time as an experiment is run. However, these are not picked up well by fourier transforms since edge effects can cause a large amount of frequency concentration in the lower frequencies that follow an inverse power law. In certain cases, we can also model these as transient events such as ELM, pellet injections, sawtooth crashes and disruptions. Interestingly, due to the impulse nature of an ELM, its time-frequency transform often appears as a spike since it is a broadband signature over a short period of time. The spikes in

fusion literature are often referred to as transients, since they are instantaneous events that can be modeled as deterministic changes to the plasma state.

Random stochastic processes have the property of noise being mean-centered. While many models tend to assume gaussian noise, real world signals can often contain a myriad of stochastic noise that is not purely gaussian. This can include laplacian and uniform noise with physical underpinnings ranging from thermal noise to electronics-induced noise.

Nonstationary behavior is often defined by chaotic cascading events or Brownian-like motion. This gives it unique behavior around certain energy levels, but can often lead to a dropoff in observed frequency that roughly follows Kolmogorov-type cascades or more advanced fractal patterns. This is often described in turbulence literature, as they measure the nonstationary behavior of the plasma using measurements of fractional changes to the plasma state [17]. In most literature, it is observed to follow a $1/f^\chi$ dropoff where $0 < \chi < 2$ [18]. Here, we also include integrated stochastic behavior, also known as Brownian noise, since it can be described by a stochastic process with $\chi = 2$. By characterizing $1/f$ behavior generally, we can now account for χ of any scale, even that which is measured to be greater than 2 [19]. This same frequency distribution follows that of deterministic nonperiodic signals. This is an important point to note since separating deterministic movements and nonstationary drifts is not trivial, and thus motivates us to group these two together as broad modes, since they both create broad, spanning structures in both the time-frequency domain.

Quasicoherent modes are a special class of modes more unique to Tokamak literature [20]. This is because fusion can contain phenomena that can comfortably exist between these categories as defined above. So this can fall somewhere between pure oscillation, chaotic behavior, and stochastic behavior, with modes of interest often exhibiting more coherent-like resonant structures.

Coherent and quasicoherent modes can be thought of as sharing a general category since they both involve analysis of a localized time-frequency signature just with added uncertainty for quasicoherent structures. Transient and broad events can be thought

of as another more general category where measurements of interest span a wide range of frequencies, where transients are specifically an instantaneous case without a different frequency profile; let us call these broadband measurements. Finally, stochastic measurements can be thought of as uncertain variance; note that this does not include coherent noise such as antenna scans, and such – but those require prior knowledge, so should be treated as such after being classified as a generic measurement from the previous categories.

Breaking this down into three main categories and five subcategories allows us to isolate the operations of diagnostic processing while trying to sift through signals. Research in denoising often employs some sort of averaging in coherent signals, be it on the direct signal, in between signals, or within some latent space. However, it necessitates that all other measurements that need to be removed are stochastic. Since we may have a broadband class of coherent signals, we need to first isolate them before denoising at risk of broadband signals overpowering faint, coherent signals (such as in the case of AE modes in integrated diagnostics). Therefore, our processing pipeline will first isolate the broadband signals from coherent signals, then denoise the coherent signals to extract high fidelity modes.

2.2 Time-Frequency Transformation

While wavelet decomposition and Slepian-based multitaper methods offer theoretical advantages, especially with removing broadband and coherent noise respectively, they come with interpretability drawbacks and can also result in linear removal of faint coherent modes. Therefore we utilize the short-time Fourier transform (STFT) for its computational efficiency and compatibility with existing fusion workflows e.g., MODESPEC [10, 21, 13]. First, to ensure replicability, signals on all diagnostics used are resampled to 500 kHz (8th-order Chebyshev Type I decimation with phase preservation) and processed using a Hann window ($N = 1024$, overlap=87.5%) to balance time-frequency resolution [22, 23]. All resulting spectrograms therefore span from 0 to 250kHz, which is often a good upper limit at which AE modes can

be observed [24]. Data is processed via Fusion Artificial Intelligence and Toolkit Hub (FAITH), a Python package and fusion database optimized for high performance machine learning [25]. Crucially, our downstream enhancement and extraction techniques are designed to be agnostic to the specific time-frequency representation of a signal. The processing pipeline is demonstrated in Figure 2 using an ECE channel from shot 178631.

Here, we have a real-valued time domain signal $x(t)$ with its complex STFT representation

$$Z(t, f) = \text{STFT}\{x(t)\} \quad (1)$$

and its log-power representation

$$P(t, f) = |Z(t, f)|^2 \quad (2)$$

we also define its real and imaginary components

$$R + jI = \text{Re}\{Z\} + j \text{Im}\{Z\} \quad (3)$$

Given the above class definitions, we can decompose $Z(t, f)$ into three components:

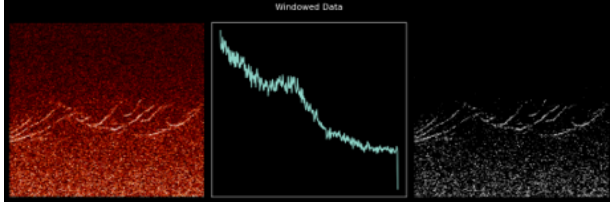
$$Z(t, f) = M(t, f) + V(t, f) + \eta(t, f) \quad (4)$$

where $M(t, f)$ are the coherent observations, $V(t, f)$ are the broadband observations, and $\eta(t, f)$ is the stochastic noise.

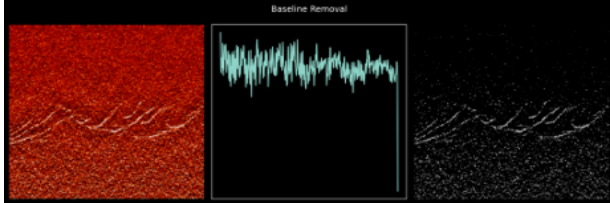
2.3 Separating Broadband Observations

Sensors that measure nonperiodic phenomena can be dominated by strong measures of turbulence or other nonstationary movements. This can result in broadband high-amplitude, structured background that can globally obscure faint coherent modes.

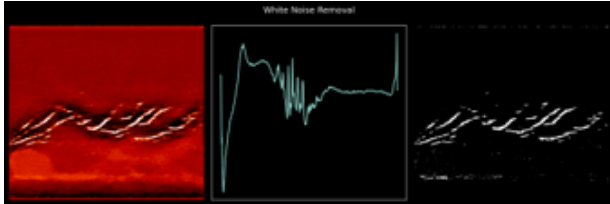
Therefore, our goal here is to separate $V(t, f)$ from $Z(t, f)$. This problem resembles that of harmonic percussive separation (HPS) in which harmonics, or horizontal, are distinct from percussive, or verticals in music [26]. However, since this type of measurement can be a mix of chaotic or random events with up to infinite correlation, it is difficult to define a single digital filter that models and extracts this based



(a) Raw spectrogram processing with characteristic low-frequency bias. Direct thresholding obscures faint AE modes.



(b) Baseline removal: The estimated broadband baseline $V(t, f)$ is subtracted to isolate coherent structures from the background, effectively whitening the signal.



(c) Multichannel denoising: The baseline-corrected spectra after self-supervised denoising reveals coherent mode structures with stochastic noise suppressed.

Figure 2: Signal processing pipeline for ECE shot 178631 demonstrating progressive separation of coherent modes from broadband background and stochastic noise. (left) Raw STFT power spectra. (center) Welch periodogram, which is the time averaged spectrogram. (right) Thresholding on power spectra.

purely on the dynamics of the time series. Stationarizing a signal or clipping the direct current (DC) bin, or that of the first order fast Fourier transform (FFT) can theoretically remove the first order trend, which helps with fit stability, but since the frequency bins follow the power law, it often has very little effect. So spectral analysis of highly dynamic diagnostics such as CO_2 often include clipping a full segment of low-frequency bins, up to a certain point such as 40kHz where the background slope becomes less extreme [27]. However, this functions at the expense of possibly losing low-frequency mode information. Therefore, a more robust method is needed in which we directly fit a filter to the energy cascade.

Turning to spectroscopy, methods have been adapted previously to address this in the purely frequency domain, modeling this background curvature as a "baseline" with signals of interest as peaks on top of the general spectral background. To isolate $V(t, f)$, we can adopt robust baseline removal techniques [28, 29]. The core of this approach is to estimate the baseline $V(f, t)$ of each FFT sample and subtract this, then divide it by the variance between the residual using an asymmetric optimizer or wavelet decomposition. This is based on event-related spectral perturbation (ERSP) which is widely used in electroencephalography (EEG) signal processing for event isolation in brains which show similar drifting behavior [30]. Removing the baseline effectively flattens the signal such that broadband structures are an independent set of measurements while coherent modes and stochastic noise are preserved. In other words, since the color of the signal is removed, the residual signal is a "whitened" form of the original signal. The baseline can be estimated by solving the following optimization problem:

$$\min_V \sum_{t,f} w(t, f) (P(t, f) - V(t, f))^2 + \lambda \sum_{t,f} |\nabla^2 V(t, f)| \quad (5)$$

where $P(t, f)$ is the observed power spectrogram, $V(t, f)$ is the estimated baseline, $w(t, f)$ is an asymmetric weight function defined as

$$w(t, f) = \begin{cases} p & \text{if } P(t, f) > V(t, f) \\ 1 - p & \text{if } P(t, f) \leq V(t, f) \end{cases} \quad (6)$$

with p typically set to 0.001 to penalize positive residuals more heavily, and λ is the smoothness parameter controlling the second-order derivative regularization term $\nabla^2 V(t, f)$. We use the standard value of $\lambda = 10^6$ for asymmetric least squares, which balances fitting fidelity with smoothness constraints to accurately capture the broadband baseline structure while preserving sharp coherent mode features.

To distinguish broadband and transient events, we simply turn to the definition of transient event and note that it demarks a transition. These broadband measurements can then be separately processed out by measuring the average impulse of time-slices in the filtered measurement if needed.

An important note is that this method is not perfect, and may contain strong edge effects on certain sensors which causes fitting error to propagate down the line. We have observed this to extend to 4kHz on our 250kHz spectra. In order to mitigate this effect, a pre-emphasis filter which follows the equation

$$P'(t, f) = P(t, f) \cdot f^\alpha \quad (7)$$

and assumes a first order inverse power law where $\alpha = 1$ is first used [31].

2.4 Separating Coherent Signals from Stochastic Noise

Following the whitening of Z , the coherent mode spectrogram $C(f, t) = M(f, t) + \eta(f, t)$ remains corrupted by stochastic white noise, η which can be comprised of various types of white noise including gaussian noise, laplacian noise, and uniform noise due to physical phenomena such as thermal noise. While numerous methods exist to mitigate noise, they present critical limitations for this specific application. Linear filters (e.g., Gaussian/Wiener filters, BM3D) tend to average out the faint, transient, and non-stationary signals we aim to preserve [32]. Conversely, sparse transforms (e.g., wavelet, curvelet) rely on strong priors regarding signal morphology, while modal decomposition techniques [e.g., empirical mode decomposition (EMD), variational mode decomposition (VMD)] are computationally prohibitive for large-scale database generation or quick intershot

analysis [33]. Multichannel methods are often used, particularly in tokamaks where it is the standard signal enhancing method before physics analysis is conducted. However, classical extensions such as singular spectrum analysis (SSA) or MUSIC scale exponentially with channel count, limiting decomposition to small time slices and also creating a strong variance tradeoff between channels that may not be completely linearly correlated [34, 35]. To address the bias-variance tradeoff, hardware approaches to denoising implements closely spaced sensors such as correlation electron cyclotron emission (CECE) which effectively provides two measures of the same phenomena [36]. However, this is not always feasible due to budget or engineering constraints. And in future fusion plants, these diagnostics may not be planned such as in SPARC or ITER [37, 38].

To address these limitations, we extend multichannel correlation—similar to the classical cross-power spectrum (CPS) using a non-linear deep learning estimator. The CPS between two signals, $x(t)$ and $y(t)$, is defined as the expected value of the raw cross-periodogram:

$$M_{xy}(f) = \mathbb{E}\{M_x(f)M_y(f)^*\} \quad (8)$$

where $M_x(f)$ and $M_y(f)$ are the STFT of two given signals [16]. The noise reduction in this method arises from the complex conjugate multiplication $M_x M_y^*$, followed by the expectation operator $\mathbb{E}\{\cdot\}$. Explicitly, the product is:

$$M_x M_y^* = (R_x R_y + I_x I_y) + i(I_x R_y - R_x I_y) \quad (9)$$

where R is the real part of M and I is the imaginary part. Under the expectation $\mathbb{E}\{\cdot\}$, incoherent random phase relationships in the noise terms cancel out, leaving only components with coherent phase relationships. However, this acts as a blind linear filter. If a transient signal event is present in only a small fraction of segments, the averaging process suppresses it by a factor of $1/M$, with added measurements. To address this, we can reframe this problem as finding the optimal predictor for one signal component given all others, in which the cosine component of the dot product acutally represents a distance pseudo-metric, which can simply be replaced with any distance function we want. This demonstration of information

transfer for diagnostic reconstruction has been previously demonstrated [39, 40]. To do so, we construct a neural-network F_θ that approximates X :

$$X'_N = \mathbb{E}[X_N | X_1, \dots, X_k] \quad (10)$$

The input is a multichannel tensor composed of the separated real and imaginary parts of the STFT from k input signals:

$$\mathbf{X}_{\text{in}}(t_m, f) = [\text{Re}\{X_1\}, \text{Im}\{X_1\}, \dots, \text{Re}\{X_k\}, \text{Im}\{X_k\}] \quad (11)$$

The U-Net F_θ maps this $2k$ -channel tensor to the 2-channel real and imaginary components of a target signal X_N :

$$\mathbf{X}_{\text{pred}}(t_m, f) = F_\theta(\mathbf{X}_{\text{in}}(t_m, f)) = [\text{Re}\{X'_N\}, \text{Im}\{X'_N\}] \quad (12)$$

The network is optimized by minimizing the mean absolute error (MAE) between the prediction and the target for robustness [41]:

$$\mathcal{L}(\theta) = \sum_{m=1}^M \sum_f \|\mathbf{X}_{\text{pred}}(t_m, f) - \mathbf{X}_{\text{target}}(t_m, f)\| \quad (13)$$

This loss forces the U-Net to learn optimal non-linear combinations of the input components to reconstruct the coherent target. Effectively, the network learns complex relationships across the T-F plane analogous to $R_x R_y + I_x I_y$. This also allows our result to be easily interpreted as the minimal distance to each input spectra given the information present in all other spectra. Conceptually, we can see the benefit of this compared to classical methods in Figure 3.

A critical concern is whether a network trained on this may learn the noise. However, developments in self-supervised denoising have demonstrated that a network trained to predict a noisy target from a noisy input can quickly result in a signal, provided the noise is zero-mean and independent [42]. The optimal function $f(\cdot)$ which minimizes the L_1 loss is the conditional expectation $f(x') = \mathbb{E}[y' | x']$. Assuming the target $y' = x + n_2$ and input $x' = x + n_1$, where n_1 and n_2 are independent noise realizations:

$$\mathbb{E}[y' | x'] = \mathbb{E}[x + n_2 | x'] = \mathbb{E}[x | x'] + \mathbb{E}[n_2 | x'] \quad (14)$$

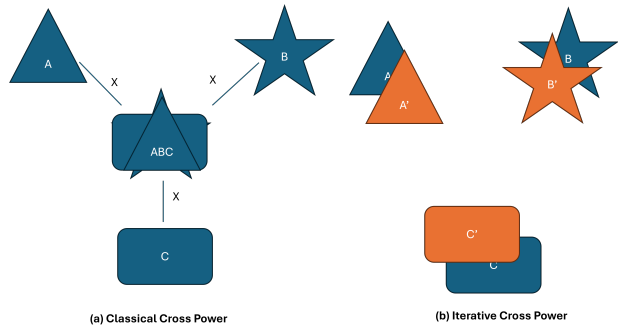


Figure 3: (left) Averaging signals can introduce a bias that removes information about each individual signal. (right) Reconstructing each channel with the information from all other channels leads to a better estimate of the true signal.

Since we can safely assume the noise n_2 is independent of the input state due to existing use of the CPS, then $\mathbb{E}[n_2 | x'] \rightarrow 0$. Note that channel prediction is performed independently for $\text{Re}(X)$ and $\text{Im}(X)$, as applying this to the real spectra will cause significantly worse results due to a loss in complex information. This method also differs from past results which have denoised spectrograms with a cross-phase interaction, since it is observed that joint denoising can introduce spectral artifacts in a similar vein as real spectrum denoising.

Another question that arises is that if we can employ this theory from self-supervised denoising, why can't we directly just use existing self-supervised image denoising algorithms on the spectra? From our tests, introducing autocorrelation-based measures seems to degrade quality. Standard single-image methods (e.g., blind-spot networks) often assume pixel-wise independence. However this assumption is violated in sparse non-linear spectra where measurement correlations span the entire time-frequency domain [43]. Methods such as AP-BSN, which uses variable kernel sizes has been tested, but has not given sufficiently good results, as sparse background noise measurements are observed to just change radius of correlated noise while removing adjacent signals [44]. An example can be seen in figure 4. An explanation for this can be that spectral signals

can be extremely sparse so there is not enough adjacent information to directly reconstruct clean signals.

Furthermore, existing autocorrelation-based self-supervised signal denoisers operating in the time domain can suffer from subsampling information loss with unsatisfactory denoising results for direct extraction of modes [45]. However, in the case that a diagnostic is highly oversampled compared to the frequency range of interest, this may be a good alternative. A strong approach to this method is presented in which the autocorrelation of subsampled time series can begin performing on a similar level to the denoising power of a cross-spectrum with decimation levels greater than 4x for CECE [46]. Therefore, there is no reason to believe that the iterative method in this section can not be applied to this case. However, since the measurements DIII-D has on hand are 500kHz for ECE and 1MHz for CO₂ with spectral regions of interest extending up to 250kHz, we do not have sufficient bandwidth to apply this.

One more point to note is that the iterative method presented is not perfect as we do not have infinite noisy realizations of a single signal as in the theoretically perfect scenario. Thus, residual noise could be learned after a long amount of training with many parameters. To prevent this, we employed a total variation (TV) stopping criterion to act as a strong proxy for noise content measurement [47].

2.5 Coherent and Transient Thresholding

Next we aim to separate physical events from the background to provide a candidate mode labelset. Standard image thresholding methods such as Otsu are designed for bimodal distributions and fail on spectrograms, which are characterized by sparse, high-intensity signals with dense, low-intensity background [48]. While approximate quantile selection is common practice in fusion signal extraction, it is automatic. But to build on this heuristic, we can note that the reason a high percentage value is often chosen is because coherent and transient observations are essentially an impulse, or anomaly in a sparse time-frequency domain. Therefore, we can frame this as an anomaly detection problem using the knee point

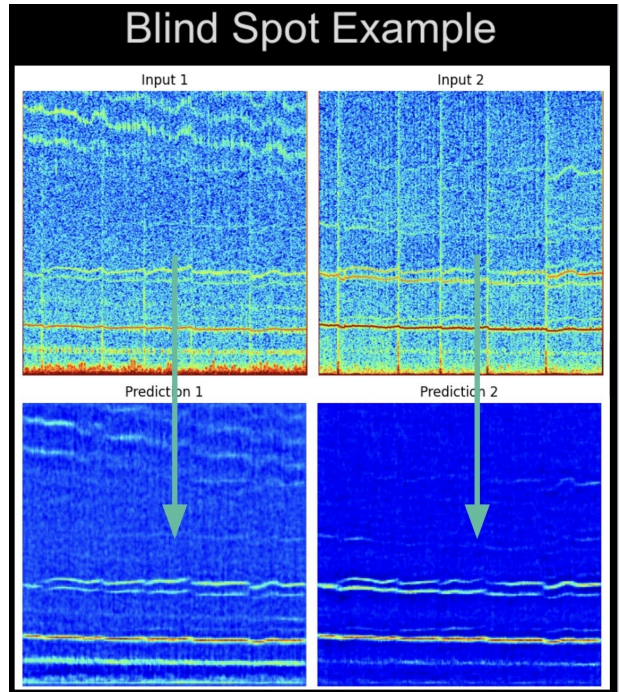


Figure 4: Blind-spot denoising example with AT-BSN, a more efficient form of AP-BSN. (top) Original spectra with small kernel. (bottom) denoised spectra with large kernel. Although noise is reduced in both cases, the small kernel method still retains largely observable measurements of noise, while the large kernel method removes fluctuations especially at the top.

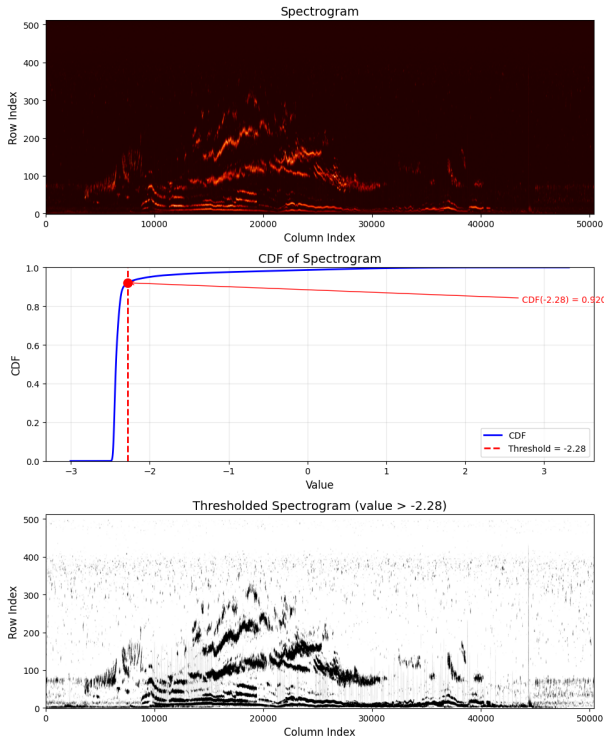


Figure 5: (Top) Original denoised spectra. (Middle) CDF with threshold set at corner. (Bottom) Thresholded spectra.

of the spectrograms cumulative distribution function (CDF) [49].

The algorithm proceeds as follows: We first recognize that all data of interest resides in the upper half of the power spectrogram. To handle the long tail of the noise distribution, all values below the spectrograms mean are set to the mean. This fixes any possible processing step that could introduce discontinuities to the image histogram such as thresholding. Next, the CDF of the resulting intensity distribution is computed and normalized. Then, the knee point of this distribution is calculated by connecting the CDF endpoints, interpolated such that both x and y axes on the CDF are equal. Then the maximum distance from the curve to the line is considered the optimal point. An example demonstration can be seen in Figure 5.

This method is parameter-free, save the level of interpolation detail wanted for tracing the CDF, and can be applied to any spectrogram, as it relies on the shape of the intensity distribution rather than absolute values. While the authors have not found this exact formulation of thresholding for spectrograms, the result is inspired by bioacoustic vocalization contour extraction where it was noticed that most of the points that meet the true positive requirement are above the cumulative distribution function [50]. Another point to address is that this is preferred due to being a global threshold, as it reduces parameterization compared to local methods. One drawback is that knee point detection necessitates the presence of a signal in a spectra. If a spectra does not contain any signal, the knee point will simply select random points in the background distribution that happen to be slightly higher than the rest. However, we do not encounter this issue as all the spectrograms we process in this paper contain at least one mode.

2.6 Detection Refinement

The automated segmentation process yields a large database of high quality candidate event masks. However, these signals may contain false negatives since channel-wise predictions may fail to predict information that is only present on one channel devoid of information on other channels.

So, to capture these edge effects, we employ multiple robust segmentation refinement techniques to improve the labeled dataset. We train a U-Net on 5-fold randomized single channel measurements of signals using a symmetric binary cross-entropy (BCE) approach [51]. We also employ data augmentations including flips and elastic deformation, treating this as an image segmentation problem [52]. A subset of high entropy measurements from the resulting average is added to the predicted signal to improve the determined space of signals.

The final result of this pipeline is a database of segmented plasma events. This leaves us a large set of about 40,000 spectrogram fragments we can map measurements to without any manual labeling.

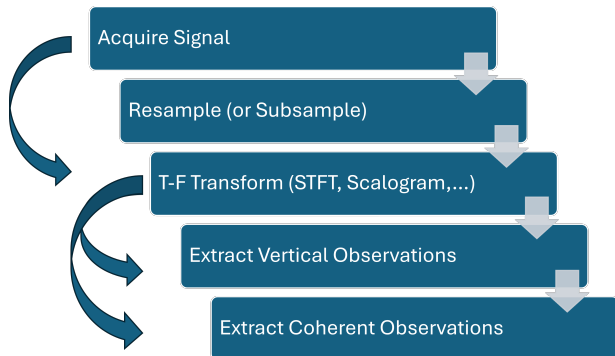


Figure 6: The automated data extraction pipeline and surrogate model training process. For real-time usage, the surrogate model can automatically extract vertical and coherent observations from signals.

2.7 Surrogate Model

Finally, a surrogate model is trained on the processed results. For the time being, we simply train a U-Net on the coherent and transient portions of the spectra, this time using more spectrogram-targeted augmentations, specifically SpecAug [53]. In order to maintain the same pipeline across channels, we find the cumulative mean and standard deviation per diagnostic, and perform normalization. Then we clip spectrograms to their 0.1 and 99.9 percentile with robust scaling [54]. To deal with parameter uncertainty, we also employ multi-period multi-scale surrogate training on bicubic resampled labels, randomly sampling from the range of window sizes [256, 2048] and hop sizes [64, 512], loosely inspired by the training regime for self-supervised waveform synthesis [55]. This improves performance robustness across a variety of signal parameter settings. Without this, the segmentations are observed to be highly sensitive to window size and overlap.

The final process can be summarized in Figure 6.

2.8 Model Architecture

In this paper, we have used a U-Net three separate times. While the training regiment is different each time, the architecture remains the same. The U-Net used is a modified architecture of the original

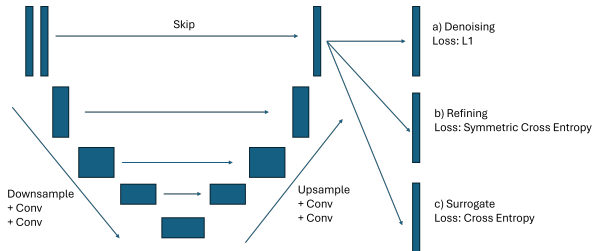


Figure 7: U-Net architecture used for all three models in this paper. For self-supervised training, the input and output are multichannel depending on the number of samples used. For robust label expansion, the input and output is one single channel. For surrogate model training, the input is single channel and the output is two channel for binary segmentation.

U-Net [52]. In upsampling, a convolutional transpose has been replaced with an upsample double convolution to prevent checkerboard artifacts [56]. Training was done using binary floating-point (BF)-16 precision. The model is shown in figure 7. While higher performing models exist now, the U-Net provides a strong baseline.

3 Results

3.1 Investigating DIII-D Spectrograms

Visualizing magnetic coil measurements in Figure 8, we see it gives clean mode identifications onto which we can project mode numbers down the line. From these segmentations, we can obtain direct amplitude measurements 1. Next, we check results on CO_2 , shown in Figure 9. Despite the strong low frequency amplitudes we are able to cleanly extract both high and low frequency structures.

We also check ECE. An interesting case study we can investigate are two shots, 199597 and 199607, from a tearing mode control experiments at DIII-D, in which 199597 exhibits tearing instability, shown in Figure 10, while 199607 is electron cyclotron current drive (ECCD) suppressed, shown in Figure 11 [57]. Since tearing modes often occur around the

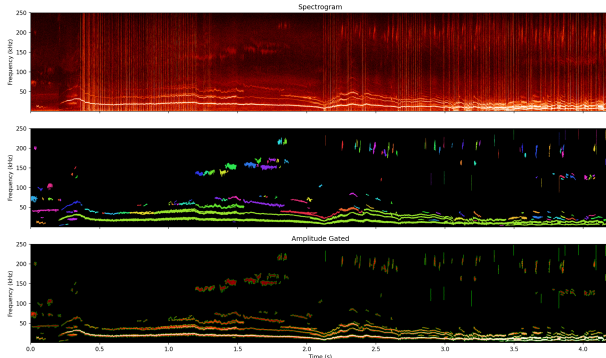


Figure 8: (top) example magnetic spectrogram for shot 170008 with only coherent mode extraction. (middle) individually extracted events using a model threshold. (bottom) gated spectrogram, which captures amplitudes of interest. transient events here can be filtered out, allowing direct coherent mode extraction.

Table 1: Database of detected signal regions.

Lbl	f_{\min} (kHz)	f_{\max} (kHz)	t_{\min} (ms)	t_{\max} (ms)	Amp. (dB)
1	7	68	183	4096	5335
3	28	96	376	2358	546
21	99	172	1295	1796	42
4	32	95	2318	2988	1026
46	264	301	1137	1316	32
			⋮		
12	47	58	3747	3781	2098
48	279	295	1075	1098	58
11	47	55	3648	3686	1794
70	361	379	3977	3989	129
92	442	504	376	379	215

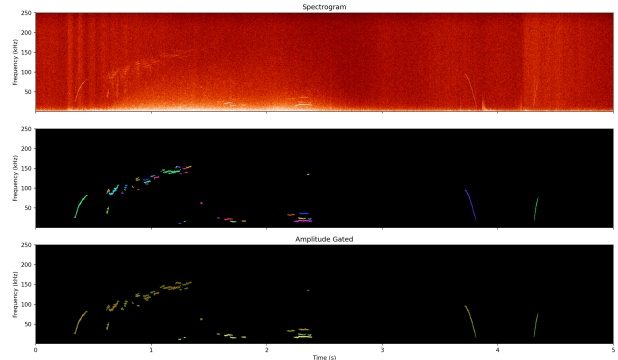


Figure 9: (top) example CO₂ density spectrogram for shot 185781. (middle) the individually extracted events using a model threshold. (bottom) gated spectrogram, which captures amplitudes of interest. Different events including alfvén-like and low frequency modes can be captured, along with very fine chirping structures.

50kHz range, we can do a general split measurement of mode amplitudes at this range and higher frequency modes. We can immediately identify a higher amount of sustained high frequency Alfvén-like modes during tearing mode suppression in addition to the upward movement of low frequency modes. In addition, we can compare this to the Shapely value-given probabilities of influence [57]. Shapely values indicate that core measurements are much more likely than edge to predict a tearing mode. If we look at edge ECE measurements, we do not observe this mode behavior, but we can observe this in the core.

3.2 Benchmarking on TJ-II Spectrograms

To test the model’s ability to generalize to other fusion devices, we deploy it on ECE spectrograms from the TJ-II stellarator in Spain. These spectrograms have different noise characteristics and event structures compared to DIII-D, making them a good test for generalizability. We obtain a recall of 0.825 on expert labeled TJ-II spectrograms, indicating strong performance even without retraining. One consistent

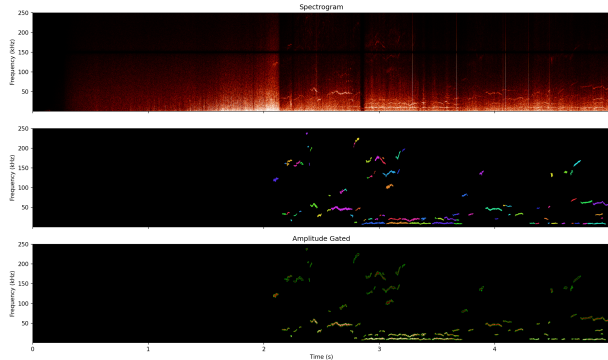


Figure 10: (top) ECE spectrogram segmentation in a tearing mode shot 199597. (middle) individually extracted events using a model threshold. (bottom) gated spectrogram, which captures amplitudes of interest. high frequency modes appear starting at 2 seconds, rapidly ending near 3.4 seconds when tearing mode occurs.

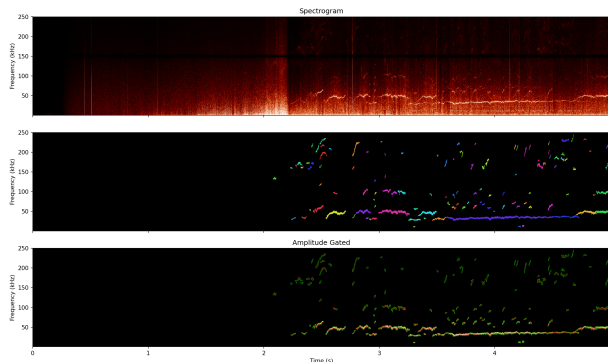


Figure 11: (top) ECE spectrogram segmentation in a tearing-suppressed shot 199607. (middle) individually extracted events using a model threshold. (bottom) gated spectrogram, which captures amplitudes of interest. high frequency modes appear starting at 2 seconds, and do not diminish as tearing mode is suppressed.

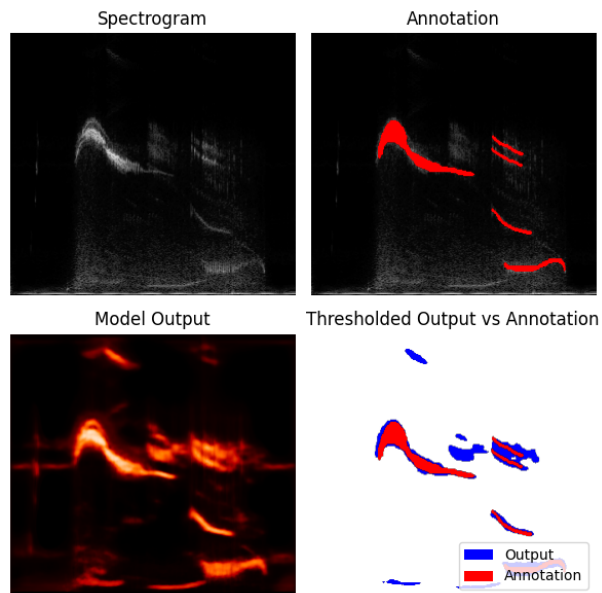


Figure 12: Example of TJ-II ECE spectrogram with expert annotations and model output. The threshold used here is the recommended 50% threshold.

issue is that the model measures the cutoff frequency at around 100kHz. However, this is a manual bias that can be corrected for in post processing similar to scan lines. Additionally, the model is able to pick up structures not annotated by the original annotation and identify well areas with no mode activity. An example is shown in Figure 12. Overall, this shows the model can generalize well to different fusion devices.

3.3 Benchmarking on Non-Fusion Datasets

To test the extent of this model’s generalizability, we deploy it on spectrograms from other domains in science. We test this on a well known Detection, Classification, Density Estimation, and Localization of Marine Mammals Using Passive Acoustics (DCLDE) 2011 Ocodonte dataset since it is a widely known benchmark for localized time frequency annotations in the presence of broadband events, in this case snapping shrimp instead of ELMs [58]. We ob-

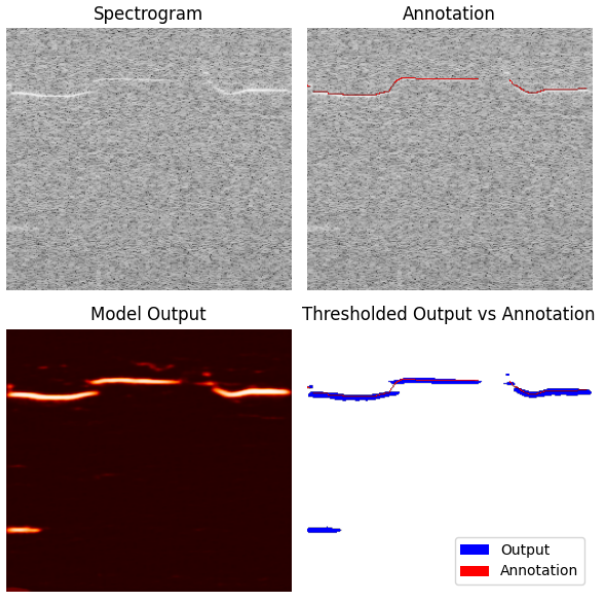


Figure 13: Example of DCLDE 2011 dolphin call spectrogram with expert annotations (top) and model output (bottom) at the recommended 50% threshold.

tain a recall of 0.7708 on *Delphinus capensis* and 0.7953 on *Delphinus delphis* which is strong for a zero-shot task. This model seems to perform well in most cases, except when pitch rapidly drops and when annotations are at the lowest frequency bins. While precision is low, this is likely due to annotations being strongly localized to 1 pixel while the model marks a wider region. Since modes in tokamaks also tend to have varying widths, this is not much of a concern for many of our application. In addition, annotations can sometimes mark the far edge of a dolphin call while the detection at the center, giving both false negative and false positive values. For this reason, skeletonization was not employed as this may cause the model to converge to a single pixel that may not overlap with the annotated signal at all, which may lead to markedly worse results. Examples can be found in Figure 13 and Figure 14.

With fine-tuning on the dataset, we expect much stronger alignment with standard benchmark goals.

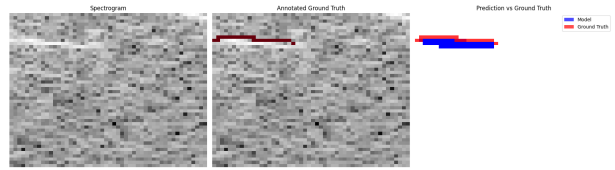


Figure 14: Example of DCLDE 2011 with missed overlap. While the general segmentation region is in the correct vicinity, there are only three pixels of overlap between annotation and model output.

This shows that the resulting model can be generalizable to domains beyond fusion for analysis.

3.4 Performance

With the given starting HDF5 Dataset format, creating a database of 5000 ready for training takes roughly 5 hours on a single Nvidia A100 graphics processing unit (GPU) and 64 core intel central processing unit (CPU).

Training a high quality surrogate semantic segmentation model with full 5 fold validation takes around 12 hours.

When running inference, it takes approximately 0.5s to process a full shot on GPU, making it suitable for active plasma monitoring. And roughly 5-10 seconds on CPU depending on the number of spectra being processed in parallel.

4 Discussion and Future Goals

We have presented a self-supervised pipeline for automated extraction of events from time-frequency spectrograms. The method combines baseline removal to separate broadband turbulence from coherent modes, U-Net-based multichannel denoising to suppress stochastic noise, thresholding for a minimal parameter segmentation procedure, and a surrogate neural network. Results show strong performance across DIII-D diagnostics (ECE, CO₂, MHR, BES), automatically reveals Alfvén-like activity during tearing mode suppression. The surrogate model generalizes well to TJ-II stellarator data and bioacoustic sig-

nals without retraining, with inference times of 0.5-10 seconds per shot suitable for tokamak inter-shot analysis.

To improve performance of the denoising run, we can combine this with a scheme closer to Self-inspired Noise2Noise for full coverage [59]. We can also improve the denoising regiment to be more architecturally efficient, following a similar blind spot method instead of predicting single channels at one time [60]. This can allow us to use many more channels without a large memory overhead.

We plan to also include information on phase and turbulence in future additions. Finally, we can extend this to extract the inherent correlation between diagnostics in one pass, as the current setup is limited to extraction of only one view at a time.

While surrogate mode extraction performs quickly on a GPU, its performance on variable size input spectra for CPUs can be significantly slower. We can investigate quantization and pruning for deployment on CPU systems in the future.

5 Acknowledgments

This material is based upon work supported by the U.S. Department of Energy, Office of Science, Office of Fusion Energy Sciences, using the DIII-D National Fusion Facility, a DOE Office of Science user facility, under Award(s) DE-FC02-04ER54698 and DE-SC0024527. The authors also gratefully acknowledge financial support from the Princeton Laboratory for Artificial Intelligence under Award 2025-97.

Special thanks to Marie Roch for providing access to the DCLDE dataset and annotations, Andres Bustos and Enrique Zapata-Cornejo for providing access to the TJ-II dataset. Thanks to Jalal Butt, Sangkyeun Kim, Ricardo Shousha, and Frederik Simons.

Disclaimer: This report was prepared as an account of work sponsored by an agency of the United States Government. Neither the United States Government nor any agency thereof, nor any of their employees, makes any warranty, express or implied, or assumes any legal liability or responsibility for the accuracy, completeness, or usefulness of any infor-

mation, apparatus, product, or process disclosed, or represents that its use would not infringe privately owned rights. Reference herein to any specific commercial product, process, or service by trade name, trademark, manufacturer, or otherwise does not necessarily constitute or imply its endorsement, recommendation, or favoring by the United States Government or any agency thereof. The views and opinions of authors expressed herein do not necessarily state or reflect those of the United States Government or any agency thereof.

References

- [1] J. S. Kim, D. H. Edgell, J. M. Greene, E. J. Strait, and M. S. Chance. MHD mode identification of tokamak plasmas from Mirnov signals. *Plasma Physics and Controlled Fusion*, 41(11):1399, November 1999.
- [2] Liu Chen and Fulvio Zonca. Physics of Alfvén waves and energetic particles in burning plasmas. *Reviews of Modern Physics*, 88(1):015008, March 2016.
- [3] G. Federici, P. Andrew, P. Barabaschi, J. Brooks, R. Doerner, A. Geier, A. Herrmann, G. Janeschitz, K. Krieger, A. Kukushkin, A. Loarte, R. Neu, G. Saibene, M. Shimada, G. Strohmayer, and M. Sugihara. Key ITER plasma edge and plasma-material interaction issues. *Journal of Nuclear Materials*, 313-316:11-22, March 2003.
- [4] A. W. Leonard. Edge-localized-modes in tokamak(s). *Physics of Plasmas*, 21(9):090501, September 2014.
- [5] R. M. Churchill, C. S. Chang, J. Choi, R. Wang, S. Klasky, R. Kube, H. Park, M. J. Choi, J. S. Park, M. Wolf, R. Hager, S. Ku, S. Kampel, T. Carroll, K. Silber, E. Dart, and B. S. Cho. A Framework for International Collaboration on ITER Using Large-Scale Data Transfer to Enable Near-Real-Time Analysis. *Fusion Science and Tech-*

- nology*, 77(2):98–108, February 2021. eprint: <https://doi.org/10.1080/15361055.2020.1851073>.
- [6] Jaemin Seo, Rory Conlin, Andrew Rothstein, SangKyeun Kim, Joseph Abbate, Azarakhsh Jalalvand, and Egemen Kolemen. Multimodal Prediction of Tearing Instabilities in a Tokamak. In *2023 International Joint Conference on Neural Networks (IJCNN)*, pages 1–8, June 2023. ISSN: 2161-4407.
- [7] Nathaniel Chen, CheolSik Byun, Azarakhsh Jalalvand, SangKyeun Kim, Andrew Rothstein, Filippo Scotti, Steve L Allen, David Eldon, Keith Erickson, and Egemen Kolemen. Regulation compliant AI for fusion: Explainable image-based feedback control of divertor detachment in DIII-D tokamak. *Nuclear Fusion*, 2026.
- [8] A Bustos, E Ascasióbar, A Cappa, and R Mayo-García. Automatic identification of MHD modes in magnetic fluctuation spectrograms using deep learning techniques. *Plasma Physics and Controlled Fusion*, 63(9):095001, July 2021.
- [9] E d D Zapata-Cornejo, D Zarzoso, S D Pinches, S E Sharapov, and M Fitzgerald. Segmentation of MHD modes using Fourier transform, wavelets and computer vision algorithms. *Plasma Physics and Controlled Fusion*, 66(9):095016, August 2024.
- [10] E.d.D. Zapata-Cornejo, D. Zarzoso, S.D. Pinches, A. Bustos, A. Cappa, and E. Ascasióbar. A novel unsupervised machine learning algorithm for automatic Alfvénic activity detection in the TJ-II stellarator. *Nuclear Fusion*, 64(12):126057, October 2024.
- [11] M. E. Austin and J. Lohr. Electron cyclotron emission radiometer upgrade on the DIII-D tokamak. *Review of Scientific Instruments*, 74(3):1457–1459, March 2003.
- [12] R. E. Slusher and C. M. Surko. Study of density fluctuations in plasmas by small-angle CO₂ laser scattering. *The Physics of Fluids*, 23(3):472–490, March 1980.
- [13] E. J. Strait. Magnetic diagnostic system of the DIII-D tokamak. *Review of Scientific Instruments*, 77(2):023502, February 2006.
- [14] G. McKee, R. Ashley, R. Durst, R. Fonck, M. Jakubowski, K. Tritz, K. Burrell, C. Greenfield, and J. Robinson. The beam emission spectroscopy diagnostic on the DIII-D tokamak. *Review of Scientific Instruments*, 70(1 II):913–916, January 1999.
- [15] D. R. McCarthy. Edge harmonic oscillations produced by toroidal velocity shear. *Physics of Plasmas*, 9(6):2451–2454, June 2002.
- [16] J. S. Bendat and A. G. Piersol. Random Data Analysis and Measurement Procedures. *Measurement Science and Technology*, 11(12):1825, December 2000.
- [17] V. P. Budaev, Y. Kikuchi, M. Toyoda, Y. Uesugi, and S. Takamura. Effect of rotating helical magnetic field on the turbulence fractal structure and transport in the tokamak edge. *Journal of Nuclear Materials*, 313-316:1309–1313, March 2003.
- [18] Edoardo Milotti. 1/f noise: a pedagogical review, April 2002. arXiv:physics/0204033.
- [19] Manfred Schroeder. *Fractals, Chaos, Power Laws: Minutes from an Infinite Paradise*. Dover Publications, August 2009.
- [20] A. Mazurenko, M. Porkolab, D. Mossessian, J. A. Snipes, X. Q. Xu, and W. M. Nevins. Experimental and Theoretical Study of Quasicoherent Fluctuations in Enhanced $\{D\}_{\alpha}$ Plasmas in the Alcator C-Mod Tokamak. *Physical Review Letters*, 89(22):225004, November 2002.
- [21] Marie Farge, Kai Schneider, and Pascal Devynck. Extraction of coherent bursts from turbulent edge plasma in magnetic fusion devices using orthogonal wavelets. *Physics of Plasmas*, 13(4):042304, April 2006.

- [22] Pauli Virtanen, Ralf Gommers, Travis E. Oliphant, Matt Haberland, Tyler Reddy, David Cournapeau, Evgeni Burovski, Pearu Peterson, Warren Weckesser, Jonathan Bright, Stéfan J. van der Walt, Matthew Brett, Joshua Wilson, K. Jarrod Millman, Nikolay Mayorov, Andrew R. J. Nelson, Eric Jones, Robert Kern, Eric Larson, C. J. Carey, İlhan Polat, Yu Feng, Eric W. Moore, Jake VanderPlas, Denis Laxalde, Josef Perktold, Robert Cimrman, Ian Henriksen, E. A. Quintero, Charles R. Harris, Anne M. Archibald, Antônio H. Ribeiro, Fabian Pedregosa, and Paul van Mulbregt. SciPy 1.0: fundamental algorithms for scientific computing in Python. *Nature Methods*, 17(3):261–272, March 2020.
- [23] F.J. Harris. On the use of windows for harmonic analysis with the discrete Fourier transform. *Proceedings of the IEEE*, 66(1):51–83, January 1978.
- [24] C.E. Shannon. Communication in the Presence of Noise. *Proceedings of the IRE*, 37(1):10–21, January 1949.
- [25] PlasmaControl/FusionAIHub: A centralized platform for fusion-related machine learning workflows.
- [26] Derry FitzGerald. Harmonic/Percussive Separation Using Median Filtering. 2010.
- [27] M.A. Van Zeeland, E. Bass, X.D. Du, W.W. Heidbrink, C. Chrystal, C. Crocker, G. DeGrandchamp, S. Haskey, D. Liu, J. Gonzalez-Martin, K.E. Thome, G. Yu, and Y. Zhu. Isotope impact on Alfvén eigenmodes and fast ion transport in DIII-D. *Nuclear Fusion*, 64(5):056033, April 2024.
- [28] J. Carlos Cobas, Michael A. Bernstein, Manuel Martín-Pastor, and Pablo García Tahoces. A new general-purpose fully automatic baseline-correction procedure for 1D and 2D NMR data. *Journal of Magnetic Resonance*, 183(1):145–151, November 2006.
- [29] Sung-June Baek, Aaron Park, Young-Jin Ahn, and Jaebum Choo. Baseline correction using asymmetrically reweighted penalized least squares smoothing. *Analyst*, 140(1):250–257, December 2014.
- [30] Romain Grandchamp and Arnaud Delorme. Single-Trial Normalization for Event-Related Spectral Decomposition Reduces Sensitivity to Noisy Trials. *Frontiers in Psychology*, 2:236, September 2011.
- [31] B S Atal and Suzanne L Hanauer. Speech Analysis and Synthesis by Linear Prediction of the Speech Wave.
- [32] Kostadin Dabov, Alessandro Foi, Vladimir Katkovnik, and Karen Egiazarian. Image Denoising by Sparse 3-D Transform-Domain Collaborative Filtering. *IEEE Transactions on Image Processing*, 16(8):2080–2095, August 2007.
- [33] Konstantin Dragomiretskiy and Dominique Zosso. Variational Mode Decomposition. *IEEE Transactions on Signal Processing*, 62(3):531–544, February 2014.
- [34] Andreas Groth. Multivariate singular spectrum analysis and the road to phase synchronization. *Physical Review E*, 84(3), 2011.
- [35] K E J Olofsson, J M Hanson, D Shiraki, F A Volpe, D A Humphreys, R J La Haye, M J Lancot, E J Strait, A S Welander, E Kolemen, and M Okabayashi. Array magnetics modal analysis for the DIII-D tokamak based on localized time-series modelling. *Plasma Physics and Controlled Fusion*, 56(9):095012, July 2014.
- [36] A. E. White, L. Schmitz, W. A. Peebles, T. A. Carter, T. L. Rhodes, E. J. Doyle, P. A. Gourdain, J. C. Hillesheim, G. Wang, C. Holland, G. R. Tynan, M. E. Austin, G. R. McKee, M. W. Shafer, K. H. Burrell, J. Candy, J. C. DeBoo, R. Prater, G. M. Staebler, R. E. Waltz, and M. A. Makowski. A correlation electron cyclotron emission diagnostic and the importance of multifield fluctuation measurements for

- testing nonlinear gyrokinetic turbulence simulations). *Review of Scientific Instruments*, 79(10):103505, October 2008.
- [37] M. L. Reinke, I. Abramovic, A. Albert, K. Asai, J. Ball, J. Batko, J. Brettingen, D. Brunner, M. Cario, J. Carmichael, C. Chrobak, A. Creely, D. Cykman, M. Dalla Rosa, E. Dubas, C. Downey, A. Ferrera, J. Frenje, E. Fox-Widdows, R. Gocht, G. Gorini, R. Granetz, M. Greenwald, A. Grieve, M. Hanson, J. Hawke, T. Henderson, S. Hicks, J. Hillesheim, A. Hoffmann, I. Holmes, N. Howard, A. Hubbard, J. W. Hughes, J. Ilagan, J. Irby, M. Jean, G. Kaur, R. Kennedy, E. Kowalski, A. Q. Kuang, R. Kulchy, M. LaCapra, C. Lafleur, M. Lagieski, R. Li, Y. Lin, T. Looby, R. Zubieta Lupo, S. Mackie, E. Marmar, S. McKanas, A. Moncada, R. Mumgaard, C. E. Myers, V. Nikolaeva, M. Nocente, S. Normile, C. Novoa, S. Ouellet, E. Panontin, C. Paz-Soldan, J. Pentecost, C. Perks, M. Petruzzo, M. Quinn, J. Raimond, P. Raj, M. Rebai, V. Riccardo, D. Rigamonti, J. E. Rice, A. Rosenthal, M. Safabakhsh, A. Saltos, J. Shanahan, M. Silva Sa, I. Song, J. Souza, B. Stein-Lubrano, I. G. Stewart, R. Sweeney, M. Tardocchi, A. Tinguely, D. Vezinet, X. Wang, and J. Witham. Overview of the early campaign diagnostics for the SPARC tokamak (invited). *Review of Scientific Instruments*, 95(10):103518, October 2024.
- [38] W. Biel, R. Albanese, R. Ambrosino, M. Ariola, M. V. Berkel, I. Bolshakova, K. J. Brunner, R. Cavazzana, M. Cecconello, S. Conroy, A. Dinklage, I. Duran, R. Dux, T. Eade, S. Entler, G. Ericsson, E. Fable, D. Farina, L. Figini, C. Finotti, Th. Franke, L. Giacomelli, L. Giannone, W. Gonzalez, A. Hjalmarsson, M. Hron, F. Janky, A. Kallenbach, J. Kogoj, R. König, O. Kudlacek, R. Luis, A. Malaquias, O. Marchuk, G. Marchiori, M. Mattei, F. Maviglia, G. De Masi, D. Mazon, H. Meister, K. Meyer, D. Micheletti, S. Nowak, Ch. Piron, A. Pironti, N. Rispoli, V. Rohde, G. Sergienko, S. El Shawish, M. Siccinio, A. Silva, F. da Silva, C. Sozzi, M. Tardocchi, M. Tokar, W. Treutler, and H. Zohm. Diagnostics for plasma control – From ITER to DEMO. *Fusion Engineering and Design*, 146:465–472, September 2019.
- [39] Azarakhsh Jalalvand, Max Curie, SangKyeun Kim, Peter Steiner, Jaemin Seo, Qiming Hu, Andrew Oakleigh Nelson, and Egemen Kolemen. Diag2Diag: Multimodal super-resolution diagnostics for physics discovery with application to fusion, May 2024. arXiv:2405.05908 [physics] version: 2.
- [40] CheolSik Byun, Azarakhsh Jalalvand, Nathaniel Chen, SangKyeun Kim, Filippo Scotti, Steven L. Allen, Seungtae Oh, Yoonseong Han, Andrew Rothstein, Keith Erickson, David Eldon, H. H. Lee, and Egemen Kolemen. Real-Time Feedback Control of Radiation Front-Based Detachment Enabled by Machine Learning on DIII-D and KSTAR. November 2025.
- [41] Yeong Il Jang, Keuntek Lee, Gu Yong Park, Seyun Kim, and Nam Ik Cho. Self-supervised Image Denoising with Downsampled Invariance Loss and Conditional Blind-Spot Network. In *2023 IEEE/CVF International Conference on Computer Vision (ICCV)*, pages 12162–12171, Paris, France, October 2023. IEEE.
- [42] Jaakko Lehtinen, Jacob Munkberg, Jon Hasselgren, Samuli Laine, Tero Karras, Miika Aittala, and Timo Aila. Noise2Noise: Learning Image Restoration without Clean Data, October 2018. arXiv:1803.04189 [cs].
- [43] Hamadi Chihaoui and Paolo Favaro. Masked and Shuffled Blind Spot Denoising for Real-World Images. In *2024 IEEE/CVF Conference on Computer Vision and Pattern Recognition (CVPR)*, pages 3025–3034, June 2024.
- [44] Shiyan Chen, Jiyuan Zhang, Zhaofei Yu, and Tiejun Huang. Exploring Efficient Asymmetric Blind-Spots for Self-Supervised Denoising in Real-World Scenarios. In *2024 IEEE/CVF Conference on Computer Vision and Pattern Recognition (CVPR)*, pages 2814–2823, June 2024.

- [45] Jiasong Wu, Qingchun Li, Guanyu Yang, Lei Li, Lotfi Senhadji, and Huazhong Shu. Self-Supervised Speech Denoising Using Only Noisy Audio Signals, January 2023. arXiv:2111.00242 [eess].
- [46] Christian Yoo, Garrard D. Conway, Jacob Schellpfeffer, Rachel Bielajew, Klara Hoefler, Diego J. Cruz-Zabala, David Cusick, William Burke, Branka Vanovac, Anne E. White, and the ASDEX Upgrade Team. A novel method for thermal noise reduction, enabling measurements of broadband, low-amplitude electron temperature fluctuations using individual radiometer channels, December 2025. arXiv:2512.02244 [physics].
- [47] Leonid I. Rudin, Stanley Osher, and Emad Fatemi. Nonlinear total variation based noise removal algorithms. *Physica D: Nonlinear Phenomena*, 60(1):259–268, November 1992.
- [48] Nobuyuki Otsu. A Threshold Selection Method from Gray-Level Histograms. *IEEE Transactions on Systems, Man, and Cybernetics*, 9(1):62–66, January 1979.
- [49] Ville Satopaa, Jeannie Albrecht, David Irwin, and Barath Raghavan. Finding a "Kneedle" in a Haystack: Detecting Knee Points in System Behavior. In *2011 31st International Conference on Distributed Computing Systems Workshops*, pages 166–171, Minneapolis, MN, USA, June 2011. IEEE.
- [50] Florian Dadouchi, Cedric Gervaise, Cornel Ioana, Julien Huillery, and Jerome I. Mars. Automated segmentation of linear time-frequency representations of marine-mammal sounds. *Journal of the Acoustical Society of America*, 134(3):2546–2555, May 2013.
- [51] Yisen Wang, Xingjun Ma, Zaiyi Chen, Yuan Luo, Jinfeng Yi, and James Bailey. Symmetric Cross Entropy for Robust Learning with Noisy Labels, August 2019. arXiv:1908.06112 [cs].
- [52] Olaf Ronneberger, Philipp Fischer, and Thomas Brox. U-Net: Convolutional Networks for Biomedical Image Segmentation, May 2015. arXiv:1505.04597 [cs].
- [53] Daniel S. Park, William Chan, Yu Zhang, Chung-Cheng Chiu, Barret Zoph, Ekin D. Cubuk, and Quoc V. Le. SpecAugment: A Simple Data Augmentation Method for Automatic Speech Recognition. In *Interspeech 2019*, pages 2613–2617, September 2019. arXiv:1904.08779 [eess].
- [54] Ricardo A. Maronna, R. Douglas Martin, Victor J. Yohai, and Matías Salibián-Barrera. *Robust Statistics: Theory and Methods (with R)*. John Wiley & Sons, January 2019. Google-Books-ID: K5RxDwAAQBAJ.
- [55] Kundan Kumar, Rithesh Kumar, Thibault de Boissiere, Lucas Gestin, Wei Zhen Teoh, Jose Sotelo, Alexandre de Brebisson, Yoshua Bengio, and Aaron Courville. MelGAN: Generative Adversarial Networks for Conditional Waveform Synthesis, December 2019. arXiv:1910.06711 [eess].
- [56] Augustus Odena, Vincent Dumoulin, and Chris Olah. Deconvolution and Checkerboard Artifacts. *Distill*, 1(10):e3, October 2016.
- [57] Hiro J. Farre-Kaga, Andrew Rothstein, Rohit Sonker, SangKyeun Kim, Ricardo Shousha, Minseok Kim, Keith Erickson, Jeff Schneider, and Egemen Kolemen. Interpreting AI for Fusion: an application to Plasma Profile Analysis for Tearing Mode Stability, July 2025. arXiv:2502.20294 [physics].
- [58] Marie A. Roch, T. Scott Brandes, Bhavesh Patel, Yvonne Barkley, Simone Baumann-Pickering, and Melissa S. Soldevilla. Automated extraction of odontocete whistle contours. *The Journal of the Acoustical Society of America*, 130(4):2212–2223, October 2011.
- [59] Weisong Zhao. WeisongZhao/SN2N, November 2025. original-date: 2023-12-23T13:23:08Z.

- [60] Samuli Laine, Tero Karras, Jaakko Lehtinen, and Timo Aila. High-Quality Self-Supervised Deep Image Denoising, October 2019. arXiv:1901.10277 [cs].